

## Nanocrystalline CeO as effective adsorbent of azo dyes

Nataša M. Tomić, Zorana D. Dohčević-Mitrović, Novica M. Paunović, Dušan Ž. Mijin, Nenad D. Radić, Boško V. Grbić, Sonja M. Aškrabić, Biljana M. Babić, and Danica V. Bajuk-Bogdanović

*Langmuir*, **Just Accepted Manuscript** • Publication Date (Web): 14 Sep 2014

Downloaded from <http://pubs.acs.org> on September 26, 2014

### Just Accepted

“Just Accepted” manuscripts have been peer-reviewed and accepted for publication. They are posted online prior to technical editing, formatting for publication and author proofing. The American Chemical Society provides “Just Accepted” as a free service to the research community to expedite the dissemination of scientific material as soon as possible after acceptance. “Just Accepted” manuscripts appear in full in PDF format accompanied by an HTML abstract. “Just Accepted” manuscripts have been fully peer reviewed, but should not be considered the official version of record. They are accessible to all readers and citable by the Digital Object Identifier (DOI®). “Just Accepted” is an optional service offered to authors. Therefore, the “Just Accepted” Web site may not include all articles that will be published in the journal. After a manuscript is technically edited and formatted, it will be removed from the “Just Accepted” Web site and published as an ASAP article. Note that technical editing may introduce minor changes to the manuscript text and/or graphics which could affect content, and all legal disclaimers and ethical guidelines that apply to the journal pertain. ACS cannot be held responsible for errors or consequences arising from the use of information contained in these “Just Accepted” manuscripts.



# Nanocrystalline CeO<sub>2-δ</sub> as effective adsorbent of azo dyes

*Nataša M. Tomić<sup>§</sup>, Zorana D. Dohčević-Mitrović<sup>\*,§</sup>, Novica M. Paunović<sup>§</sup>, Dušan Ž. Mijin<sup>†</sup>,  
Nenad D. Radić<sup>‡</sup>, Boško V. Grbić<sup>‡</sup>, Sonja M. Aškrabić<sup>§</sup>, Biljana M. Babić<sup>#</sup> and Danica V.  
Bajuk-Bogdanović<sup>||</sup>*

<sup>§</sup>Institute of Physics, University of Belgrade, Pregrevica 118, 11080 Belgrade, Serbia

<sup>†</sup>Faculty of Technology and Metallurgy, University of Belgrade, Karnegijeva 4, 11000  
Belgrade, Serbia

<sup>‡</sup>ICHM, Department of Catalysis and Chemical Engineering, University of Belgrade,  
Njegoševa 12, 11000 Belgrade, Serbia

<sup>#</sup>Institute of nuclear sciences “Vinča”, University of Belgrade, 11001 Belgrade, Serbia

<sup>||</sup>Faculty of Physical Chemistry, University of Belgrade, Studentski Trg 12-16, 11000  
Belgrade, Serbia

## ABSTRACT

Ultrafine CeO<sub>2-δ</sub> nanopowder, prepared by a simple and cost effective self-propagating room temperature synthesis method (SPRT), showed high adsorption capability for removal of different azo dyes. Batch type of adsorption experiments with fixed initial pH value were conducted for the removal of Reactive Orange 16 (RO16), Methyl Orange (MO), and Mordant Blue 9 (MB9). The equilibrium adsorption data were evaluated using Freundlich and Langmuir isotherm models. The Langmuir model slightly better describes isotherm data for RO16 and MO, whereas the Freundlich model was found to best fit the isotherm data for MB9 over the whole concentration range. The maximum adsorption capacities, determined from isotherm data for MO, MB9 and RO16 were 113, 101 and 91 mg g<sup>-1</sup> respectively. The

1  
2  
3 adsorption process follows the pseudo-second-order kinetic model indicating the coexistence  
4  
5 of chemisorption and physisorption. The mechanism of azo dye adsorption is also discussed.  
6  
7

8  
9 KEYWORDS: CeO<sub>2</sub> nanoparticles, Adsorption, Reactive azo dyes, Adsorption isotherms,  
10  
11 Adsorption kinetics  
12

## 13 14 INTRODUCTION

15  
16 Synthetic dyes are widely used in a number of industries such as textile and leather industries,  
17  
18 paper printing, cosmetics, and pharmaceuticals. It is estimated to be more than 10000  
19  
20 commercially available dyes with over  $7 \times 10^5$  tons of dye-stuff produced annually.<sup>1,2</sup> Azo  
21  
22 dyes represent about 60-70% of the dyes used in textile industry. Some of them show aquatic  
23  
24 toxicity or allergenic effects and under reductive conditions they produce aromatic amines  
25  
26 that are carcinogenic.<sup>2,3</sup> Azo dyes represent a class of synthetic, colored, organic compounds,  
27  
28 which are characterized by the presence of one or more azo bonds. These dyes belong to the  
29  
30 most toxic ones compared to other forms of dyes.<sup>1</sup> Large quantities of these dyes (10-15% of  
31  
32 the total world production) are released into the waste water (typical concentration 10-200  
33  
34 mg L<sup>-1</sup>), the presence of which poses a major threat to the aquatic organisms as well as  
35  
36 animals and humans because of their nonbiodegradability, toxicity and potential carcinogenic  
37  
38 nature.<sup>4-6</sup>  
39  
40  
41  
42

43 Dye removal from textile effluents is a major environmental problem because of the  
44  
45 difficulty to treat such streams by conventional physicochemical and biological treatment  
46  
47 methods. The methods such as filtration, coagulation, flocculation, ion exchange,  
48  
49 photocatalytic degradation are unsatisfactory for wastewater treatment because are expensive  
50  
51 and may produce more toxic by-products. Among the various available water treatment  
52  
53 techniques, adsorption is the most reliable and efficient technique for dye removal, despite a  
54  
55 fact that usually the adsorbent needs to be regenerated what increases the cost of the process  
56  
57  
58  
59  
60

1  
2  
3 and can be time-consuming procedure. The liquid phase adsorption has been shown to be an  
4  
5 efficient way for removing the suspended solids, organic matter, and oil from aqueous  
6  
7 solutions. Adsorption appears to offer the best perspective over all the other treatments  
8  
9 because can handle fairly large flow rates producing a high quality effluent and does not  
10  
11 result in the formation of harmful substances, such as ozone and free radicals which are  
12  
13 present during the photodegradation process using UV.  
14  
15

16 Activated carbon is the most widely used adsorbent for this purpose, because it has a  
17  
18 high surface area and high capacity for adsorption of organic matter, but its use is limited  
19  
20 because of its high production cost and significant problems with the regeneration of the  
21  
22 spent activated carbon.<sup>7,8</sup> A great variety of low-cost biomass materials,<sup>9-13</sup> have been used to  
23  
24 produce activated carbon for the treatment of wastewaters. In recent years low cost  
25  
26 agricultural wastes are investigated as potential biosorbents,<sup>14</sup> but most of these cheap  
27  
28 substitutes have to be subjected to the process of carbonization which increases process costs.  
29  
30 Therefore, there is still a high demand for cheaper adsorbent materials with high adsorption  
31  
32 capacity.  
33  
34  
35

36 Nowadays, nanoscience and nanotechnology play important role in environmental  
37  
38 protection. There is a strong need to develop simple and economical methods for producing  
39  
40 nanomaterials with higher adsorption rates which can efficiently remove various  
41  
42 contaminants. Nanomaterials with high surface area are the most promising candidates as  
43  
44 adsorbents in organic dye removal.<sup>5, 15-19</sup>  
45  
46

47 Among various metal oxide semiconductors, CeO<sub>2</sub> is widely used in many application  
48  
49 areas such as catalysis, fuel cells, sensors, and UV shielding, owing to its outstanding  
50  
51 physical and chemical properties. The application of ceria as effective sorbent is not so often  
52  
53 studied. There are few reports in which it is demonstrated that ceria is effective sorbent for  
54  
55 the removal of high toxic pollutants such as<sup>17</sup> As(V) and Cr(VI) and azo dyes such as Congo  
56  
57  
58  
59  
60

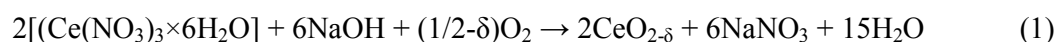
1  
2  
3 red<sup>18</sup> or Acid orange<sup>4</sup> from water. The adsorption experiments, performed on removing of  
4  
5 Reactive Orange 16 and Methyl Orange from wastewaters, mainly used as adsorbent waste  
6  
7 biomass,<sup>20</sup> various types of sludge and biosorbents.<sup>1, 13, 14, 20-26</sup> Although most of these  
8  
9 sorbents were relatively cheap and effective in dye removal they showed modest and rarely  
10  
11 high sorption capacities. On the other side to the best of our knowledge there is almost no  
12  
13 study which concerns the adsorption of Mordant Blue 9.  
14  
15

16  
17 Herein is presented the adsorption capability of ceria nanoparticles for removal of  
18  
19 different azo dyes such as Reactive Orange 16, Methyl Orange, and Mordant Blue 9. Ceria  
20  
21 nanopowder, obtained by simple and cost effective method, has shown very high efficiency  
22  
23 towards azo dye removal and has been proven to be a promising alternative for wastewater  
24  
25 treatment.  
26  
27

## 28 **EXPERIMENTAL**

### 29 **1.1 Materials preparation**

30  
31 The ultrafine CeO<sub>2-δ</sub> nanopowder was fabricated by a simple and economical self-propagating  
32  
33 room temperature synthesis method (SPRT).<sup>27, 28</sup> Starting reactants were cerium nitrate  
34  
35 hexahydrate (Ce(NO<sub>3</sub>)<sub>3</sub>×6H<sub>2</sub>O) (Acros Organics 99.5%) and sodium hydroxide (Carlo Erba).  
36  
37 Hand-mixing of nitrate with NaOH was performed in alumina mortar for ~10 min until  
38  
39 mixture got light brown. After being exposed to air for 4 h, the mixture was suspended in  
40  
41 water. Rinsing of NaNO<sub>3</sub> was performed in centrifuge at 3500 rpm for 10 min. This  
42  
43 procedure was performed four times with distilled water and twice with ethanol. The  
44  
45 precipitate was dried at 60 °C overnight. The reaction based on the self-propagating room  
46  
47 temperature method can be written as follows:  
48  
49  
50  
51



## 1.2 Characterization methods

X-ray powder diffraction (XRD) data of the sample were collected on a Siemens D-5000 diffractometer with Cu K $\alpha$  radiation over the  $2\theta$  range from 20° to 80°. Atomic force microscope (AFM) image was taken using the Omicron B002645 SPM PROBE VT AFM 25 in non-contact mode at room temperature. The powder specific surface area of the sample was calculated following the multipoint BET procedure on Quantachrome ChemBet-3000 setup. The pore size distribution was derived from nitrogen adsorption-desorption isotherm obtained at 77 K. The infrared transmission spectra (IR) of CeO<sub>2- $\delta$</sub>  pellets before and after dyes adsorption were measured on a Thermo Nicolet 6700 Fourier transform infrared spectrophotometer at room temperature. Micro-Raman spectra were collected in the backscattering configuration using the TriVista 557 Raman system. The 488 nm line of an Ar<sup>+</sup>/Kr<sup>+</sup> mixed gas laser was used as an excitation source. In order to avoid sample heating, the incident laser power on the samples was kept below 20 mW. Surface charge (zeta potential) of ceria nanoparticles at different pH was measured using Zetasizer Nano ZS90 (Malvern Instruments). Suspensions were prepared using deionized water as dispersing medium and were ultrasonicated for 15 min prior to the measurements using an ultrasonic bath. The pH values of suspensions were adjusted by adding HCl and NaOH solutions to the starting suspension of CeO<sub>2- $\delta$</sub>  nanopowder.

## 1.3 Adsorption experiments

The adsorption experiments were carried out as batch tests in a magnetically stirred thermostated glass vessel with three different concentrations (50, 100 and 200 mg L<sup>-1</sup>) of Reactive Orange 16 (RO16), Methyl Orange (MO), and Mordant Blue 9 (MB9). All measurements were performed at initial pH values of 6.2, 6 and 4.6 for MO, MB9 and RO16 dye solutions respectively. The suspensions were stirred for two minutes at room temperature

1  
2  
3 in the dark. The adsorption capacity (for the 200 mg L<sup>-1</sup> concentration of dyes) of coconut-  
4 based powdered activated carbon (PAC), of large specific surface area (1200 m<sup>2</sup>/g), was  
5 determined for comparison. The working volume (25 mL) and the quantity of ceria  
6 nanopowders and PAC (50 mg) were kept fixed in all adsorption experiments. At fixed  
7 contact time the samples were taken, centrifuged and analyzed on Shimadzu 1700 UV-VIS  
8 spectrophotometer within the spectral range where maximum of absorption for each dye  
9 occurs. In Table S1 (see Supporting Information) are given the chemical structure and the  
10 wavelength of maximal absorption ( $\lambda_{\text{max}}$ ) for each dye.  
11  
12  
13  
14  
15  
16  
17  
18  
19  
20  
21

## 22 RESULTS AND DISCUSSION

23  
24 The powder XRD pattern of CeO<sub>2- $\delta$</sub>  nanopowder is presented in Figure 1a. Diffraction peaks,  
25 corresponding to cubic fluorite structure are clearly observed. All XRD peaks are broadened  
26 indicating that the crystallites size is within the nanometer range. The average size of CeO<sub>2- $\delta$</sub>   
27 nanocrystals, estimated by Wiliamson-Hall method<sup>29</sup> is about 6 nm. Non-contact AFM image  
28 of CeO<sub>2- $\delta$</sub>  sample (Inset of Figure 1b) shows small and agglomerated non-porous CeO<sub>2- $\delta$</sub>   
29 particles. The pores between agglomerated CeO<sub>2- $\delta$</sub>  nanoparticles are also visible on the AFM  
30 image. Particle size distribution obtained from the AFM image of CeO<sub>2- $\delta$</sub>  sample is presented  
31 in the Figure 1b and was modeled by asymmetric double sigmoidal function. The average  
32 particle size is 11.4 nm.  
33  
34  
35  
36  
37  
38  
39  
40  
41  
42  
43

44 To determine the surface area and pore size distribution, nitrogen adsorption-  
45 desorption isotherms at 77 K are recorded and given in the inset of Figure 1c. According to  
46 the IUPAC classification,<sup>30</sup> nitrogen adsorption-desorption isotherm is attributed to the  
47 Langmuir IV type. The pore-size distribution was determined from the desorption branch of  
48 the isotherms using the BJH (Barett-Joyner-Halenda) method and is shown in Figure 1c. It  
49 can be observed that the sample has bimodal PSD in the mesoporous area with the first mode  
50  
51  
52  
53  
54  
55  
56  
57  
58  
59  
60

peak around 2 nm and the second one in the range 3-4 nm. The value of the BET specific surface area ( $S_{\text{BET}}$ ) is  $74 \text{ m}^2 \text{ g}^{-1}$ .

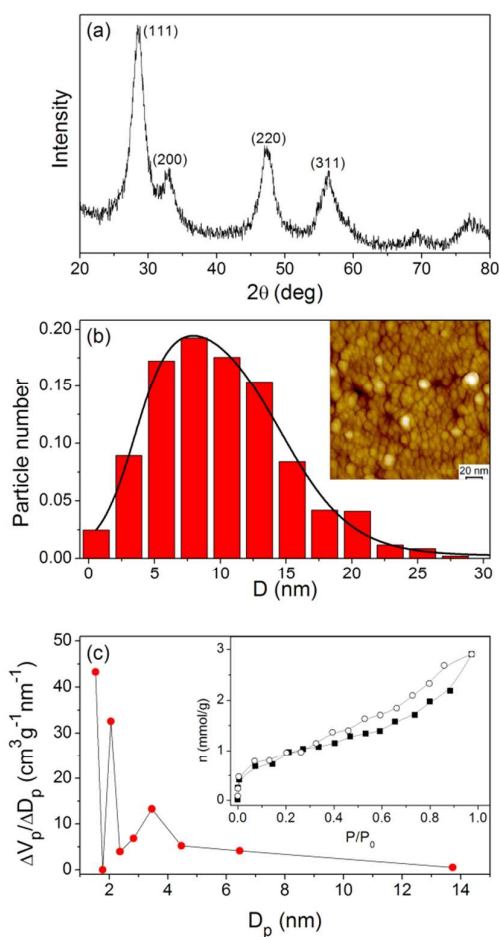
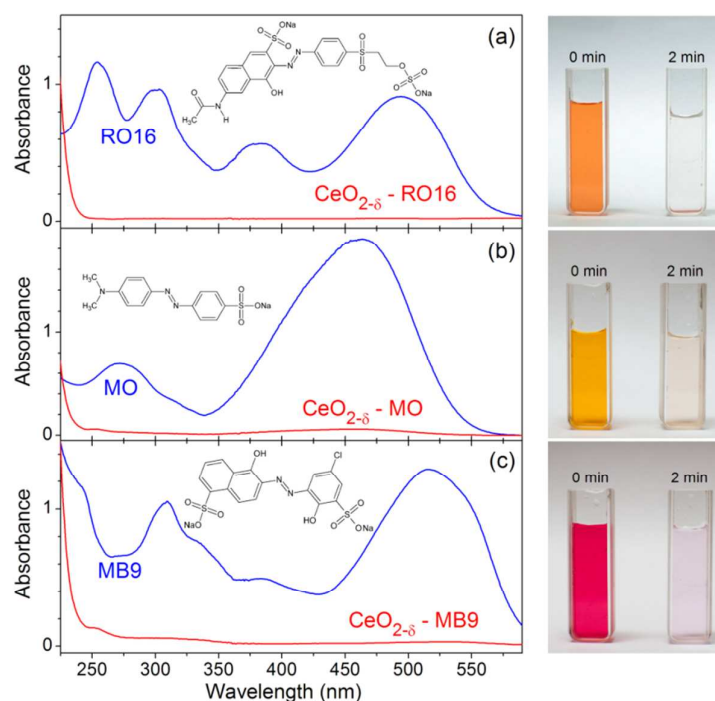


**Figure 1.** XRD spectrum (a), particle size distribution obtained from AFM (b) and pore size distribution curve obtained from the desorption branch of the isotherm (c) for  $\text{CeO}_{2-\delta}$  nanopowder. The insets present AFM image and the nitrogen adsorption-desorption isotherm of  $\text{CeO}_{2-\delta}$  nanopowder.

Further, we examined the performances of  $\text{CeO}_{2-\delta}$  nanopowder as a potential adsorbent for removal of RO16, MO, and MB9. The adsorption measurements were carried out with three different concentrations of the dye solutions ( $50$ ,  $100$  and  $200 \text{ mg L}^{-1}$ ) and absorption spectra of the dye solutions were collected after certain time interval. The UV-VIS spectrum of RO16 is given in Figure 2a (blue line) for the concentration of  $50 \text{ mg L}^{-1}$ . The



1  
2  
3 absorption spectrum of RO16 in the presence of  $\text{CeO}_{2-\delta}$  nanoparticles after two minutes is  
4 also presented in Figure 2a (red line). As can be seen, the RO16 characteristic bands  
5 decreased promptly, indicating that RO16 was removed from the solution. The corresponding  
6 photo image (right panel of Figure 2a) shows that the solution is almost colourless. The  
7  
8  
9  
10 photo image (right panel of Figure 2a) shows that the solution is almost colourless. The  
11  
12 absorption spectra of the MO and MB9 before (blue line) and after two minutes (red line) in  
13  
14 the presence of  $\text{CeO}_{2-\delta}$  nanoparticles are given in Figure 2b,c. Absorption spectra of these two  
15  
16 dye solutions after two minutes showed that the dyes were present in a very low  
17  
18 concentration. From the photo images (right panel of Figure 2b,c) it can be noticed that the  
19  
20 solutions were almost colorless after two minutes. The experiment was repeated with an  
21  
22 increased concentration for all three dyes ( $100 \text{ mg L}^{-1}$ ) and the obtained results were similar.  
23  
24  
25  
26  
27



28  
29  
30  
31  
32  
33  
34  
35  
36  
37  
38  
39  
40  
41  
42  
43  
44  
45  
46  
47  
48  
49  
50  
51 **Figure 2.** Absorption spectra with corresponding photo images of (a) RO16, (b) MO and (c)  
52 MB9 dye solutions ( $50 \text{ mg L}^{-1}$ ) before and two minutes after introducing  $\text{CeO}_{2-\delta}$  nanoparticles  
53  
54 ( $2 \text{ g L}^{-1}$ ). Mass of adsorbent= $50 \text{ mg}$ ; solution volume= $25 \text{ mL}$ .  
55  
56  
57  
58  
59  
60

1  
2  
3 The concentration of RO16 in the solution was further increased to 200 mg L<sup>-1</sup>. The  
4 absorption spectra of RO16 dye solution in the presence of CeO<sub>2-δ</sub> nanoparticles, presented in  
5 Figure S1a (Supporting Information), demonstrates that CeO<sub>2-δ</sub> quickly removes the RO16  
6 from the solution. After 40 min the equilibrium state was reached. The adsorption  
7 measurements were also performed on the solutions of MO and MB9 (200 mg L<sup>-1</sup>) in the  
8 presence of CeO<sub>2-δ</sub> nanopowder, in order to compare the efficiency of adsorption process  
9 onto ceria nanopowder for all three dyes. The adsorption capacity of CeO<sub>2-δ</sub> nanopowder was  
10 determined from the mass balance relationship:<sup>1, 13, 15, 22</sup>

$$q_e = \frac{(C_0 - C_e) \cdot V}{m} \quad (2)$$

21  
22 where  $q_e$  represents the amount of dye adsorbed per unit mass of adsorbent (mg g<sup>-1</sup>),  $C_0$  and  
23  $C_e$  are the initial and equilibrium liquid phase concentrations (mg L<sup>-1</sup>),  $V$  is the volume of the  
24 solution (L) and  $m$  is the mass (g) of CeO<sub>2-δ</sub> used.

25  
26 The adsorption rate and the amount of adsorbed dye with contact time for the solutions of  
27 RO16, MO and MB9 (200 mg L<sup>-1</sup>) are illustrated in Figure 3a,b. As can be noticed from  
28 Figure 3a,b, for all three curves is characteristic that the adsorption process is rapid in the  
29 initial stage, whereas in the later stage becomes much slower. The adsorption rate for RO16  
30 was higher at the beginning, but after 60 min much better elimination of MO from the  
31 solution was observed, whereas the adsorption rate of MB9 was still lower. The equilibrium  
32 was achieved after 40 (60) min for RO16 (MO), whereas for MB9 it was achieved after 180  
33 min. The adsorption capacities of CeO<sub>2-δ</sub> nanopowder in the case of MO, MB9 and RO16  
34 were 100, 94 and 91 mg g<sup>-1</sup>, respectively.

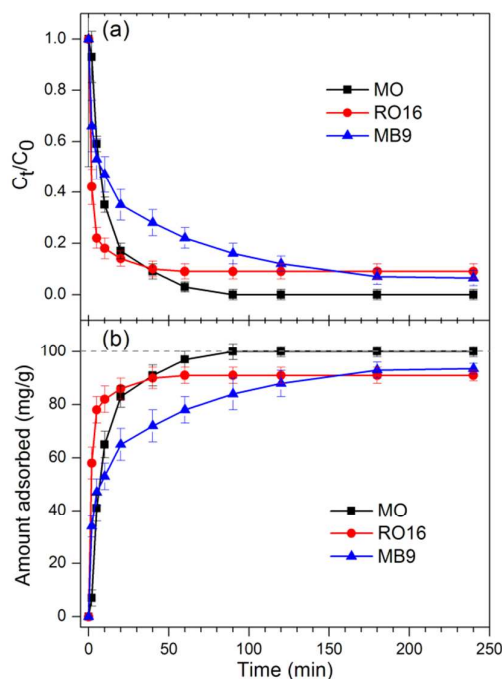


**Figure 3.** Adsorption rate (a) and amount of adsorbed dyes (b) for the solutions of MO, RO16 and MB9 ( $200 \text{ mg L}^{-1}$ ) in the presence of  $\text{CeO}_{2-\delta}$  nanopowder. Mass of adsorbent=50 mg; solution volume=25 mL.

The adsorption capacity of  $\text{CeO}_{2-\delta}$  nanopowder was compared to activated carbon. The adsorption capacity of commercial activated carbon (50 mg) is presented in Figure 4a,b,c for MO, RO16 and MB9 solutions ( $200 \text{ mg L}^{-1}$ ), respectively. In the case of MO dye solution, it can be noticed that at the beginning of the adsorption process the activated carbon was slightly faster than  $\text{CeO}_{2-\delta}$  nanopowder and reached the equilibrium state after 20 min. After 60 min both curves overlapped. In the case of RO16 dye solution, activated carbon was much slower compared to  $\text{CeO}_{2-\delta}$ . After 40 min,  $\text{CeO}_{2-\delta}$  nanopowder reached equilibrium and eliminated almost 90% of RO16 from the solution, whereas activated carbon needed two hours to reach the final adsorption capacity of  $85 \text{ mg g}^{-1}$  which was still lower than that of ceria nanopowder ( $91 \text{ mg g}^{-1}$ ). The adsorption capability of  $\text{CeO}_{2-\delta}$  for MB9 is lower than for activated carbon, although after two hours the final adsorption capacities were comparable.

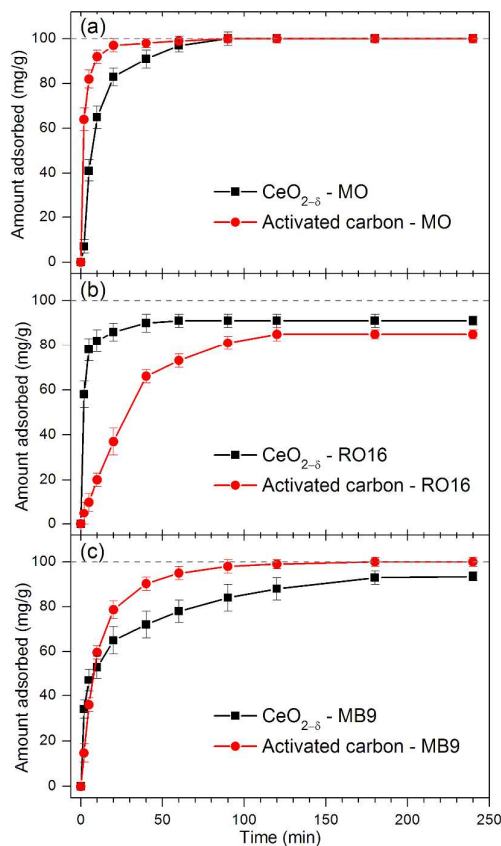


**Figure 4.** Comparison of adsorption capacities between CeO<sub>2-δ</sub> nanopowder and activated carbon in the case of (a) MO, (b) RO16 and (c) MB9 dye solutions (200 mg L<sup>-1</sup>). Mass of adsorbent=50 mg; solution volume=25 mL.

In Figure 5a-c are shown the IR transmission spectra of pure dyes and CeO<sub>2-δ</sub> nanopowders after dye adsorption. For comparison, the IR spectrum of pure CeO<sub>2-δ</sub> nanopowder is also given in Figure 5a-c.

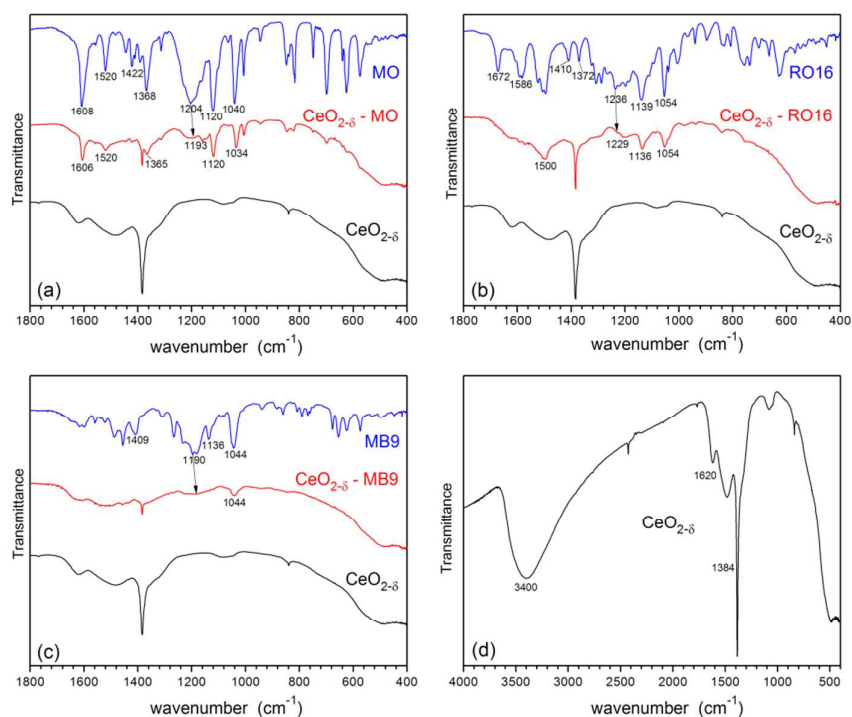


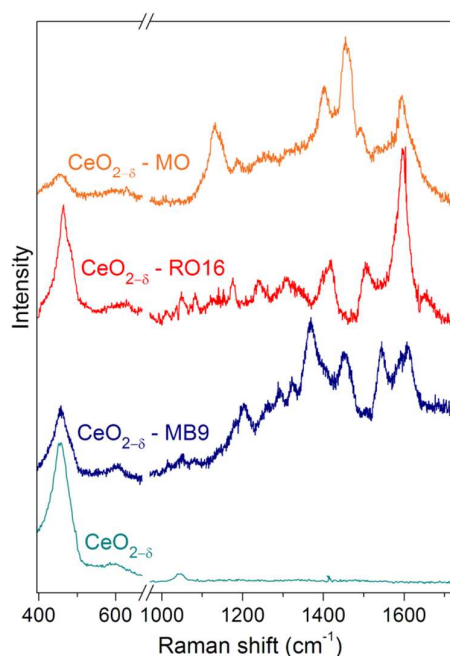
**Figure 5.** IR transmission spectra of (a) MO, (b) RO16, (c) MB9 adsorbed on the CeO<sub>2-δ</sub> together with the transmission spectra of pure dyes and CeO<sub>2-δ</sub> nanopowder and (d) IR transmission spectrum of CeO<sub>2-δ</sub> nanopowder in the extended range.

The IR spectra of pure dyes have some common characteristic bands.<sup>4, 6, 31-36</sup> The bands at 1040/1120 cm<sup>-1</sup> in MO, 1054/1139 cm<sup>-1</sup> in RO16 and 1044/1136 cm<sup>-1</sup> in MB9 originate from the symmetric stretching vibrations of SO<sub>3</sub><sup>-</sup> group ( $\nu_s(\text{SO}_3^-)$ ). The band at 1204 cm<sup>-1</sup> in MO, 1236 cm<sup>-1</sup> in RO16 and 1190 cm<sup>-1</sup> in MB9 presents the asymmetric stretching vibrations of SO<sub>3</sub><sup>-</sup> group ( $\nu_{as}(\text{SO}_3^-)$ ). The band at 1368 cm<sup>-1</sup> in MO and 1372 cm<sup>-1</sup> in RO16 belongs to the C–N stretching vibrations. The bands at 1422, 1410 and 1409 cm<sup>-1</sup> in MO, RO16, and MB9 respectively, are assigned to the N=N stretching vibrations. The bands at 1520/1608 cm<sup>-1</sup> in MO and 1586 cm<sup>-1</sup> in RO16 are from the aromatic ring stretching vibrations. The band at 1672 cm<sup>-1</sup> in the spectra of RO16 originates from the stretching vibrations of the carbonyl C=O group.

1  
2  
3 In the IR spectrum of MO dye adsorbed on CeO<sub>2-δ</sub> (shown in Figure 5a) the IR bands  
4 of the MO dye are of much lower intensity. The pronounced changes of the IR bands  
5 characteristic for sulfonate stretching vibration mode are observed. The ν<sub>as</sub>(SO<sub>3</sub><sup>-</sup>) band at  
6 1204 cm<sup>-1</sup>, is much weaker after MO adsorption on CeO<sub>2-δ</sub> and shifted to ~1193 cm<sup>-1</sup> (marked  
7 with arrow on Figure 5a). The ν<sub>s</sub>(SO<sub>3</sub><sup>-</sup>) band at 1040 cm<sup>-1</sup> in MO is slightly shifted to 1034  
8 cm<sup>-1</sup> (marked with arrow on Figure 5a) in the CeO<sub>2</sub>-MO spectrum, intensity of which is much  
9 lower after adsorption. All these changes can indicate that the sulfonate group is strongly  
10 involved in the adsorption of MO onto the CeO<sub>2-δ</sub>.<sup>34</sup> In the IR spectrum of RO16 adsorbed  
11 onto CeO<sub>2-δ</sub> (Figure 5b), a significant intensity decrease of the IR bands at 1054/1139 cm<sup>-1</sup>  
12 and 1500 cm<sup>-1</sup>, characteristic for SO<sub>3</sub><sup>-</sup> group and N-H bending vibrations,<sup>4,6</sup> is observed too.  
13 Many other bands which belong to pure RO16 dye are much weaker or barely visible in the  
14 CeO<sub>2-δ</sub>-RO16 spectrum, as for instance the band at 1410 cm<sup>-1</sup> for N=N stretching vibrations.  
15 The carbonyl C=O peak at 1672 cm<sup>-1</sup> in the IR spectrum of RO16, is almost absent from the  
16 CeO<sub>2-δ</sub>-RO16 spectrum. The ν<sub>s</sub>(SO<sub>3</sub><sup>-</sup>) band is shifted from 1139 cm<sup>-1</sup> to 1136 cm<sup>-1</sup> in the  
17 CeO<sub>2-δ</sub>-RO16 spectrum. In the IR spectrum of CeO<sub>2-δ</sub>-MB9 (Figure 5c), a major decrease of  
18 the MB9 band intensities is observed and the slight shift of asymmetric ν<sub>s</sub>(SO<sub>3</sub><sup>-</sup>) band is  
19 barely visible (marked with arrow on Figure 5c). All this indicates that RO16 and MB9 are  
20 also strongly adsorbed onto CeO<sub>2-δ</sub> surface. In Figure 5d is presented the IR transmission  
21 spectrum of pure CeO<sub>2-δ</sub> in the extended spectral range. As can be seen, strong bands near  
22 3400 cm<sup>-1</sup> and 1620 cm<sup>-1</sup> are attributed to the adsorbed H<sub>2</sub>O and hydroxyls.<sup>37,38</sup> The  
23 absorption band at 1384 cm<sup>-1</sup> originates from a CO<sub>2</sub> molecule vibrations.  
24  
25  
26  
27  
28  
29  
30  
31  
32  
33  
34  
35  
36  
37  
38  
39  
40  
41  
42  
43  
44  
45  
46  
47  
48  
49  
50

51 Raman spectra, obtained on CeO<sub>2-δ</sub> nanopowder before and after the dyes adsorption  
52 are presented in Figure 6 and are consistent with the IR measurements. In the Raman spectra  
53 of nanocrystalline CeO<sub>2-δ</sub> treated with dyes, besides the F<sub>2g</sub> mode of pure CeO<sub>2-δ</sub> positioned at  
54 ~456.5 cm<sup>-1</sup> and mode at ~600 cm<sup>-1</sup> which belongs to intrinsic oxygen vacancies,<sup>39</sup> additional  
55  
56  
57  
58  
59  
60

1  
2  
3 modes are observed. These new modes correspond to the vibrations of different atomic  
4  
5 groups of dye molecules, such as  $-N=N-$ ,  $-C=O$ ,  $-S=O$ ,  $-O-H$  and aromatic ring vibrations.  
6  
7  
8 The most prominent mode frequencies deduced from the spectra of ceria treated with MO,  
9  
10 RO16 and MB9 are summarized in the Table S2 (see Supporting Information). As the  
11  
12 majority of the atomic group vibrations characteristic for the dye molecules in question are  
13  
14 observed in the Raman spectra of dyed ceria nanopowder, it can be concluded that in all three  
15  
16 cases the adsorption of dye molecules took place.  
17  
18  
19



20  
21  
22  
23  
24  
25  
26  
27  
28  
29  
30  
31  
32  
33  
34  
35  
36  
37  
38  
39  
40  
41 **Figure 6.** Room temperature Raman spectra of  $CeO_{2-\delta}$  nanopowder before and after  
42  
43 adsorption of MO, RO16, and MB9 dyes.  
44  
45  
46  
47

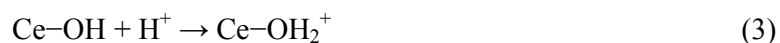
48  
49 The IR and Raman spectra unambiguously showed that MO, RO16 and MB9 are  
50  
51 adsorbed on  $CeO_{2-\delta}$  surface. In addition, from the IR spectra of three azo dyes adsorbed on  
52  
53  $CeO_{2-\delta}$  nanopowders, we concluded that  $\nu_{as}$  and  $\nu_s$  bands of sulfonate group are affected  
54  
55 considerably. The intensity ratio of these bands ( $\nu_{as}(SO_3^-)/\nu_s(SO_3^-)=0.4$ ) for adsorbed MO  
56  
57 onto ceria is different from the same ratio in the spectrum of isolated MO  
58  
59  
60

1  
2  
3 ( $\nu_{as}(\text{SO}_3^-)/\nu_s(\text{SO}_3^-)=0.9$ ). The changes of the  $\nu_{as}$  and  $\nu_s$  band intensities of sulfonate group are  
4  
5 also registered in the IR spectra of adsorbed RO16 and MB9 onto ceria. It is further worth  
6  
7 mentioning that the frequency difference  $\Delta\nu_{as-s}$  ( $\nu_{as}(\text{SO}_3^-)-\nu_s(\text{SO}_3^-)$ ) in the MO, RO16 and  
8  
9 MB9 spectra is higher than in the corresponding spectra of adsorbed dyes on ceria (see Figure  
10  
11 5). This is characteristic of the bidentate type coordination according to the Deacon and  
12  
13 Phillips<sup>40</sup> empirical rule and Bauer's<sup>41</sup> work, formed when OH groups situated on the surface  
14  
15 metal cations are substituted with oxygen atoms from azo dyes. Ji et al.<sup>44</sup> noticed similar  
16  
17 changes to ours in the IR spectra of acid orange adsorbed onto  $\text{CeO}_2$  surface and proposed  
18  
19 that bidentate type bridge is formed between sulfonate group and  $\text{Ce}^{4+}$  cations. According to  
20  
21 the observed changes in the IR spectra of MO, RO16 and MB9 adsorbed on  $\text{CeO}_{2-\delta}$   
22  
23 nanopowder it is reasonable to assume that all three dyes form bidentate type bridge on ceria  
24  
25 surface, where two oxygen atoms of the  $\text{SO}_3^-$  group are bound to one or two  $\text{Ce}^{4+}$  cations in a  
26  
27 process that involves the substitution of surface coordinated OH groups on  $\text{Ce}^{4+}$  cations  
28  
29 with oxygen atoms from azo dyes.  
30  
31  
32  
33  
34

35 Another very important factor for dyes removal concerns the capability of  $\text{CeO}_{2-\delta}$   
36  
37 nanopowders to easily form oxygen vacancies on the surface which accompany functional  
38  
39 groups. The surface functional groups can interact with dye molecules via hydrogen bonds  
40  
41 and/or electrostatic forces promoting the adsorption of dye molecules. The first principle  
42  
43 density functional theory calculations performed by Yang et al.<sup>42</sup> have shown that in oxygen  
44  
45 deficient ceria, the adsorbed water molecules prefer to decompose near the oxygen vacancy  
46  
47 site forming surface hydroxyls, where H atoms are bonded with surface oxygen atoms.  
48  
49 Therefore, they concluded that in reduced ceria both adsorbed  $\text{H}_2\text{O}$  and surface hydroxyls  
50  
51 coexist. Their calculations are in good agreement with experimental work of Kundakovic et  
52  
53 al.<sup>43</sup> performed on oxidized and reduced  $\text{CeO}_2$  thin films, who detected surface hydroxyls  
54  
55 only in reduced ceria films.  
56  
57  
58  
59  
60



Having in mind that our ceria is oxygen deficient, it is reasonable to assume that hydroxyl groups, already observed in the IR spectra, are present on the surface of  $\text{CeO}_{2-\delta}$  nanopowder. The experimental determination of the pH value at zero point charge ( $\text{pH}_{\text{ZPC}}$ ) revealed that  $\text{CeO}_{2-\delta}$  has  $\text{pH}_{\text{ZPC}} = 6.3$  (Figure S2 Supporting Information). As pH values of the dye solutions are lower than  $\text{pH}_{\text{ZPC}}$  of  $\text{CeO}_{2-\delta}$ , (see section 1.3),  $\text{CeO}_{2-\delta}$  as adsorbent acts as a positive surface. The electrostatic attraction between ceria nanoparticles and negatively charged dye ions is operable mechanism. In that case, the ceria surface hydroxyls are protonated:



In aqueous solution the sulfonate groups ( $\text{R-SO}_3\text{Na}$ ) dissociate and are converted to anionic dye ions. The adsorption process further proceeds due to the electrostatic attraction between these two oppositely charged ions:

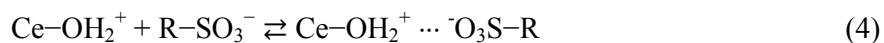
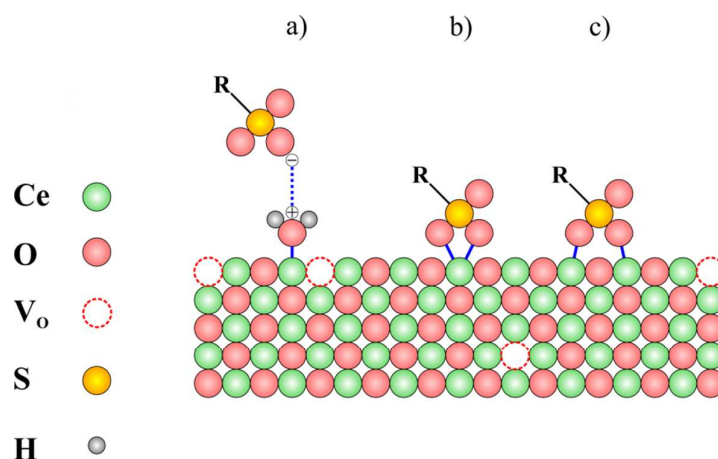


Illustration of the adsorption mechanisms between dye molecules and  $\text{CeO}_{2-\delta}$  adsorbent is shown in Figure 7.



**Figure 7.** Schematic representation of RO16, MO and MB9 adsorption on  $\text{CeO}_{2-\delta}$  surface. (a) electrostatic interaction between protonated ceria surface and sulfonate group in the dye molecule; (b) and (c) bidentate type structures between sulfonate group and  $\text{Ce}^{4+}$  cations.

1  
2  
3 As we stated earlier, the adsorption rate at the beginning of the process (presented in  
4 Figure 3a) is higher for RO16 than for MO and MB9. The difference in removal efficiency  
5 between three dyes can be explained by the fact that the pH value of the RO16 solution is  
6 close to the pH value where ceria net positive charge surface has maximum, whereas the pH  
7 values of MO and MB9 dye solutions are close to the  $\text{pH}_{\text{ZPC}}$  value of  $\text{CeO}_{2-\delta}$ . Therefore, the  
8 electrostatic interaction between RO16 dye molecules and  $\text{CeO}_{2-\delta}$  at the beginning will be  
9 stronger than for MB9 and MO. It is important to emphasize that sulfonic groups, which  
10 dissociate in aqueous solution and convert to  $\text{R-SO}_3^-$  anions, are negatively charged even at  
11 higher acidic solutions, because their  $\text{pK}_a$  values are lower than zero.<sup>44</sup> Finally, the  
12 interaction between OH groups on the surface of  $\text{CeO}_{2-\delta}$  and NH groups of the RO16 is also  
13 possible mechanism for RO16 dye adsorption<sup>19</sup> and can explain higher adsorption rate in the  
14 case of RO16 at the beginning of the process.  
15  
16  
17  
18  
19  
20  
21  
22  
23  
24  
25  
26  
27  
28

29 The study of the adsorption equilibrium isotherm is helpful in determining the  
30 maximum adsorption capacity of adsorbent for given adsorbate. These isotherms relate the  
31 dye uptake per unit mass of adsorbent,  $q_e$ , to the equilibrium liquid phase concentration  $C_e$ . In  
32 Figure 8a-c are presented the adsorption isotherms for RO16, MO and MB9 dye solutions,  
33 measured at room temperature. Adsorption isotherms were analyzed according to Langmuir  
34 and Freundlich models in order to determine the best-fit model. Langmuir's model predicts  
35 the monolayer coverage of the adsorbate, assuming that all adsorption sites are identical and  
36 energetically equivalent, whereas the Freundlich's model assumes the adsorption on  
37 heterogeneous surface composed of non-identical adsorption sites with different energy of  
38 adsorption. The isotherm equations and isotherm parameters for both models are listed in  
39 Supporting Information Table S3.  
40  
41  
42  
43  
44  
45  
46  
47  
48  
49  
50  
51  
52  
53  
54  
55  
56  
57  
58  
59  
60

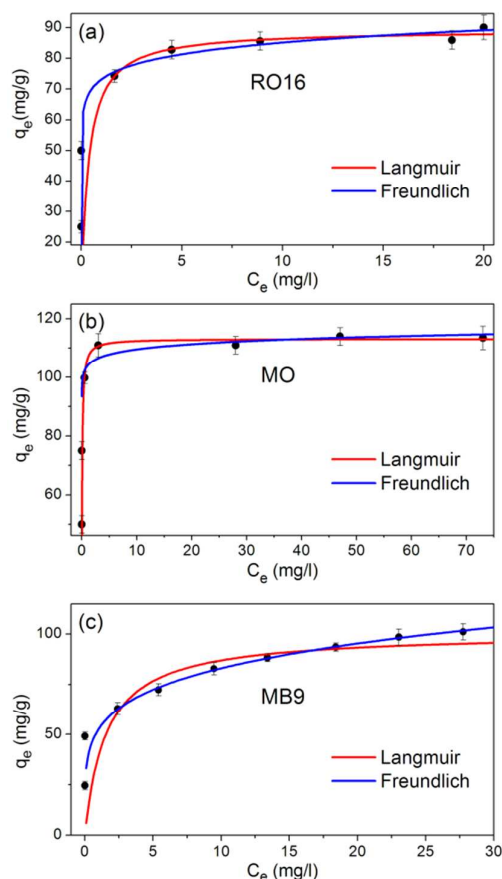


**Figure 8.** Adsorption isotherms of (a) RO16, (b) MO and (c) MB9 dye solutions on  $\text{CeO}_{2-\delta}$  at room temperature. Initial dye concentration=50-230  $\text{mg L}^{-1}$ ; mass of adsorbent=50 mg; solution volume=25 mL.

The adsorption isotherms of RO16 and MO from Figure 8a,b can be fitted by both Langmuir and Freundlich equation. Both models give reasonable good fit in the case of MO and RO16, although the values of correlation coefficients (Supporting Information Table S3) are slightly higher for Langmuir isotherm. The sorption data of MB9 are much better represented by the Freundlich model (Figure 8c and Supporting Information Table S3) which expresses adsorption in a multilayer manner on an energetically heterogenous surface.

The parameter  $1/n$  from Freundlich equation characterizes the heterogeneity of the site energies and the adsorption intensity i.e. the degree of nonlinearity of adsorption

1  
2  
3 isotherm. In their work, Tseng et al.<sup>45</sup> have defined a favorable level for the adsorption  
4  
5 isotherm curves and gave a classification for the values of parameter  $1/n$ . Despite the fact that  
6  
7 the Langmuir model seems more suitable to describe the sorption of MO and RO16 onto  
8  
9 ceria, according to Tseng's classification, the parameter  $1/n$  (listed in Supporting Information  
10  
11 Table S3) lies in the range of strongly favorable (for RO16 and MO) and favorable (for MB9)  
12  
13 adsorption. Therefore, having in mind that oxygen-deficient surface of nanosized ceria is  
14  
15 more heterogenous than homogenous, it is reasonable to conclude that adsorption of MB9,  
16  
17 MO and RO16 on  $\text{CeO}_{2-\delta}$  nanopowders reflects the presence of more than one kind of  
18  
19 adsorbent–adsorbate surface interaction. The maximal adsorption capacity values of  $\text{CeO}_{2-\delta}$   
20  
21 nanopowder from isotherm data were found to be 113, 101 and 91  $\text{mg g}^{-1}$  in the case of MO,  
22  
23 MB9 and RO16 respectively.  
24  
25  
26

27  
28 To illustrate the mechanism of adsorption, pseudo-first and pseudo-second order  
29  
30 models were used to simulate the adsorption data for various contact time from Figure 3b.  
31  
32 The pseudo-first model didn't give a good fit of the experimental data and will be omitted in  
33  
34 further discussion. Kinetic data were further analyzed with the pseudo-second-order kinetic  
35  
36 model shown in Figure 9. The linear form of the pseudo-second order model is expressed as  
37  
38 follows:  
39

$$\frac{t}{q_t} = \frac{1}{k_2 q_e^2} + \frac{t}{q_e} \quad (4)$$

40  
41  
42  
43  
44 where  $q_e$  and  $q_t$  refer to the amount of adsorbed dye at equilibrium and at time  $t$  and  $k_2$  is the  
45  
46 equilibrium rate constant of the pseudo-second order kinetic model. The linear plots of  $t/q_t$  vs.  
47  
48  $t$  (Figure 9) show that the experimental data agree well with the pseudo-second-order kinetic  
49  
50 model for all three dyes. The values of  $q_e$  and  $k_2$  were calculated from the slope and intercept  
51  
52 of Eq. (4) and their values are given in Table 1, together with experimental  $q_e$  values and  
53  
54 correlation coefficients. Calculated  $q_e$  values, tabulated in Table 1, are in quite good  
55  
56 agreement with experimental ones and the correlation coefficients have large values  
57  
58  
59  
60

( $R^2 > 0.99$ ). It can be concluded that the adsorption of MO, RO16 and MB9 on  $\text{CeO}_{2-\delta}$  nanopowder follows the pseudo-second-order kinetic model which relies on the assumption that chemisorption and effective electrostatic interaction play a major role in the adsorption process.<sup>46, 47</sup> Comparing the adsorption capacities of  $\text{CeO}_{2-\delta}$  nanopowder with other adsorbents mentioned in the introductory part, we can conclude that  $\text{CeO}_{2-\delta}$  nanopowder, produced by cost-effective SPRT method, shows efficient adsorption properties and is a promising candidate for environmentally friendly adsorbents in water treatment.

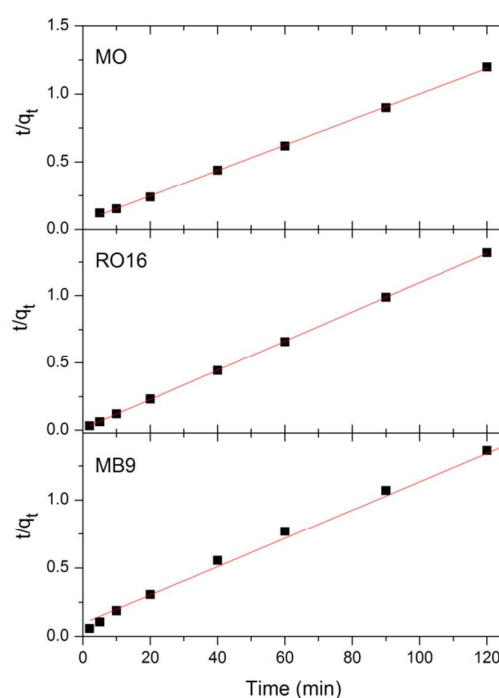


**Figure 9.** Pseudo-second-order kinetics of MO, RO16 and MB9 onto  $\text{CeO}_{2-\delta}$  nanopowder.

Initial dye concentration =  $200 \text{ mg L}^{-1}$ ; mass of adsorbent =  $50 \text{ mg}$ ; solution volume =  $25 \text{ mL}$ .

**Table 1.** Pseudo-second-order kinetic model parameters together with experimental  $q_e$  values for adsorption of each dye.

	$q_{e, cal} (\text{mg g}^{-1})$	$q_{e, exp} (\text{mg g}^{-1})$	$k_2 (\text{g mg}^{-1} \text{min}^{-1})$	$R^2$
MO	106.3	100	$1.44 \times 10^{-3}$	0.9994
RO16	100	91	$9.09 \times 10^{-3}$	0.9999
MB9	96.3	93.6	$1.13 \times 10^{-3}$	0.9977

## CONCLUSIONS

The CeO<sub>2-δ</sub> nanopowder, synthesized by facile and cost effective SPRT method, appeared to be very effective sorbent for the MO, RO16, and MB9 azo dyes. The adsorption process was monitored at fixed initial pH value, varying dyes concentration and contact time. Infrared and Raman spectroscopy measurements confirmed that the adsorption of azo dyes on CeO<sub>2-δ</sub> surface took place. The experimental adsorption data for the MO and RO16 were slightly better fitted with Langmuir isotherm, whereas Freundlich isotherm was better for MB9 over the whole concentration range. According to the values of Freundlich constant ( $1/n$ ) the adsorption of MB9, MO and RO16 lies in a favorable and strongly favorable zone. The highest adsorption capacity of CeO<sub>2-δ</sub> was obtained for the MO (113 mg g<sup>-1</sup>) and then for the MB9 (101 mg g<sup>-1</sup>) and RO16 (91 mg g<sup>-1</sup>). The formation of bidentate type bridge between sulfonate group and Ce<sup>4+</sup> cations and the protonation of ceria surface hydroxyls can be responsible for effective adsorption process. Adsorption of MO, RO16, and MB9 dyes follow the pseudo-second order equation with good correlation. These results imply that besides strong electrostatic sorption, chemisorption mechanism may play an important role for the dye adsorption. Based on our results, ceria nanopowder prepared by SPRT method, represents an effective dye adsorbent and can be a promising substitute in wastewater treatment.

## AUTHOR INFORMATION

### Corresponding Author

\*E-mail address: zordoh@ipb.ac.rs

### Notes

The authors declare no competing financial interest.

## ACKNOWLEDGEMENT

We thank to Bojan S. Stojadinović for the AFM image and Bojan Calija for the zeta potential measurements. This work was financially supported by the Serbian Ministry of Education, Science and Technological Development under the projects ON171032 and III45018 and bilateral project Serbia-Italy No. RS13MO11.

## REFERENCES

- (1) Lee, J. W.; Choi, S. P.; Thiruvengkatachari, R.; Shim, W. G.; Moon, H. Evaluation of the performance of adsorption and coagulation processes for the maximum removal of reactive dyes. *Dyes Pigments* **2006**, *69* (3), 196-203.
- (2) Gomez, V.; Larrechi, M. S.; Callao, M. P. Kinetic and adsorption study of acid dye removal using activated carbon. *Chemosphere* **2007**, *69* (7), 1151-1158.
- (3) Silva, J. P.; Sousa, S.; Rodrigues, J.; Antunes, H.; Porter, J. J.; Goncalves, I.; Ferreira-Dias, S. Adsorption of acid orange 7 dye in aqueous solutions by spent brewery grains. *Sep. Purif. Technol.* **2004**, *40* (3), 309-315.
- (4) Ji, P. F.; Zhang, J. L.; Chen, F.; Anpo, M. Study of adsorption and degradation of acid orange 7 on the surface of CeO<sub>2</sub> under visible light irradiation. *Appl. Catal. B-Environ.* **2009**, *85* (3-4), 148-154.
- (5) Venkatesha, T. G.; Viswanatha, R.; Nayaka, Y. A.; Chethana, B. K. Kinetics and thermodynamics of reactive and vat dyes adsorption on MgO nanoparticles. *Chem. Eng. J.* **2012**, *198*, 1-10.
- (6) Sahasrabudhe, M.; Pathade, G. Biodegradation of azo dye C.I. Reactive Orange 16 by an actinobacterium *Georgenia* sp. CC-NMPT-T3. *Int. J. Adv. Res.* **2013**, *1* (7), 91-99.
- (7) Mohan, D.; Pittman Jr, C. U. Activated carbons and low cost adsorbents for remediation of tri- and hexavalent chromium from water. *J. Hazard. Mater.* **2006**, *137* (2), 762-811.
- (8) Pollard, S. J. T.; Fowler, G. D.; Sollars, C. J.; Perry, R. Low-cost adsorbents for waste and wastewater treatment: a review. *Sci. Total Environ.* **1992**, *116* (1-2), 31-52.
- (9) Amin, N. K. Removal of direct blue-106 dye from aqueous solution using new activated carbons developed from pomegranate peel: Adsorption equilibrium and kinetics. *J. Hazard. Mater.* **2009**, *165* (1-3), 52-62.
- (10) Sharma, Y. C.; Uma; Upadhyay, S. N. Removal of a Cationic Dye from Wastewaters by Adsorption on Activated Carbon Developed from Coconut Coir. *Energy Fuels* **2009**, *23* (6), 2983-2988.
- (11) Aygün, A.; Yenisoy-Karakaş, S.; Duman, I. Production of granular activated carbon from fruit stones and nutshells and evaluation of their physical, chemical and adsorption properties. *Microporous Mesoporous Mater.* **2003**, *66* (2-3), 189-195.
- (12) Kannan, N.; Sundaram, M. M. Kinetics and mechanism of removal of methylene blue by adsorption on various carbons—a comparative study. *Dyes Pigments* **2001**, *51* (1), 25-40.
- (13) Annadurai, G.; Juang, R. S.; Lee, D. J. Use of cellulose-based wastes for adsorption of dyes from aqueous solutions. *J. Hazard. Mater.* **2002**, *92* (3), 263-274.

- 1  
2  
3 (14) Haddadian, Z.; Shavandi, M. A.; Abidin, Z. Z.; Fakhru'l-Razi, A.; Ismail, M. H. S.  
4 Removal Methyl Orange from Aqueous Solutions Using Dragon Fruit (*Hylocereusundatus*)  
5 Foliage. *Chem Sci Trans.* **2013**, *2* (3), 900-910.
- 6 (15) Cheung, W. H.; Szeto, Y. S.; Mckay, G. Enhancing the adsorption capacities of acid  
7 dyes by chitosan nano particles. *Bioresource Technol.* **2009**, *100* (3), 1143-1148.
- 8 (16) Wu, C. H. Adsorption of reactive dye onto carbon nanotubes: Equilibrium, kinetics and  
9 thermodynamics. *J. Hazard. Mater.* **2007**, *144* (1-2), 93-100.
- 10 (17) Zhong, L. S.; Hu, J. S.; Cao, A. M.; Liu, Q.; Song, W. G.; Wan, L. J. 3D flowerlike  
11 ceria micro/nanocomposite structure and its application for water treatment and CO removal.  
12 *Chem. Mater.* **2007**, *19* (7), 1648-1655.
- 13 (18) Ouyang, X. W.; Li, W.; Xie, S. L.; Zhai, T.; Yu, M. H.; Gan, J. Y.; Lu, X. H.  
14 Hierarchical CeO<sub>2</sub> nanospheres as highly-efficient adsorbents for dye removal. *New J. Chem.*  
15 **2013**, *37* (3), 585-588.
- 16 (19) Zhai, T.; Xie, S. L.; Lu, X. H.; Xiang, L.; Yu, M. H.; Li, W.; Liang, C. L.; Mo, C. H.;  
17 Zeng, F.; Luan, T. G.; Tong, Y. X. Porous Pr(OH)<sub>3</sub> Nanostructures as High-Efficiency  
18 Adsorbents for Dye Removal. *Langmuir* **2012**, *28* (30), 11078-11085.
- 19 (20) Won, S. W.; Yun, H. J.; Yun, Y.-S. Effect of pH on the binding mechanisms in  
20 biosorption of Reactive Orange 16 by *Corynebacterium glutamicum*. *J. Colloid Interface Sci.*  
21 **2009**, *331* (1), 83-89.
- 22 (21) Won, S. W.; Choi, S. B.; Yun, Y.-S. Performance and mechanism in binding of  
23 Reactive Orange 16 to various types of sludge. *Biochem. Eng. J.* **2006**, *28* (2), 208-214.
- 24 (22) Janaki, V.; Vijayaraghavan, K.; Ramasamy, A. K.; Lee, K. J.; Oh, B. T.; Kamala-  
25 Kannan, S. Competitive adsorption of Reactive Orange 16 and Reactive Brilliant Blue R on  
26 polyaniline/bacterial extracellular polysaccharides composite-A novel eco-friendly polymer.  
27 *J. Hazard. Mater.* **2012**, *241*, 110-117.
- 28 (23) Suteu, D.; Zaharia, C.; Malutan, T. Removal of orange 16 reactive dye from aqueous  
29 solutions by waste sunflower seed shells. *J. Serb. Chem. Soc.* **2011**, *76* (4), 17.
- 30 (24) Zhao, D.; Zhang, W.; Chen, C.; Wang, X. Adsorption of Methyl Orange Dye Onto  
31 Multiwalled Carbon Nanotubes. *Procedia Environ. Sci.* **2013**, *18* (0), 890-895.
- 32 (25) Saha, T. K.; Bhounik, N. C.; Karmaker, S.; Ahmed, M. G.; Ichikawa, H.; Fukumori, Y.  
33 Adsorption of Methyl Orange onto Chitosan from Aqueous Solution. *J. Water Resource and*  
34 *Protection* **2010**, *2*, 8.
- 35 (26) Ai, L.; Zhang, C.; Meng, L. Adsorption of Methyl Orange from Aqueous Solution on  
36 Hydrothermal Synthesized Mg–Al Layered Double Hydroxide. *J. Chem. Eng. Data* **2011**, *56*  
37 (11), 4217-4225.
- 38 (27) Yu, X.; Li, F.; Ye, X.; Xin, X.; Xue, Z. Synthesis of Cerium(IV) Oxide Ultrafine  
39 Particles by Solid-State Reactions. *J. Am. Ceram. Soc.* **2000**, *83* (4), 964-966.
- 40 (28) Boskovic, S.; Djurovic, D.; Dohcevic-Mitrovic, Z.; Popovic, Z.; Zinkevich, M.;  
41 Aldinger, F. Self-propagating room temperature synthesis of nanopowders for solid oxide  
42 fuel cells (SOFC). *J. Power Sources* **2005**, *145* (2), 237-242.
- 43 (29) Zhou, X.-D.; Huebner, W. Size-induced lattice relaxation in CeO<sub>2</sub> nanoparticles. *Appl.*  
44 *Phys. Lett.* **2001**, *79* (21), 3512-3514.
- 45 (30) Lowell, S. *Characterization of Porous Solids and Powders: Surface Area, Pore Size*  
46 *and Density*; Kluwer Academic Publishers: Dordrecht, The Netherlands, 2004.
- 47 (31) Jia, T.-J.; Song, G.; Li, P.-W.; He, T.-C.; Mo, Y.-J.; Cui, Y.-T. Vibrational modes study  
48 of methyl orange using SERS-measurement and the DFT method. *Mod. Phys. Lett. B* **2008**,  
49 *22* (29), 2869-2879.
- 50 (32) Sathiyabama, J.; Rajendran, S.; Selvi, J. A.; Amalraj, A. J. Methyl orange as corrosion  
51 inhibitor for carbon steel in well water. *Indian. J. Chem. Techn.* **2008**, *15* (5), 462-466.
- 52  
53  
54  
55  
56  
57  
58  
59  
60



1  
2  
3 (33) Liu, Y.; Sun, D. Z. Development of Fe<sub>2</sub>O<sub>3</sub>-CeO<sub>2</sub>-TiO<sub>2</sub>/gamma-Al<sub>2</sub>O<sub>3</sub> as catalyst for  
4 catalytic wet air oxidation of methyl orange azo dye under room condition. *Appl. Catal. B-*  
5 *Environ.* **2007**, *72* (3-4), 205-211.

6 (34) Hua, Q.; Shi, F. C.; Chen, K.; Chang, S. J.; Ma, Y. S.; Jiang, Z. Q.; Pan, G. Q.; Huang,  
7 W. X. Cu<sub>2</sub>O-Au Nanocomposites with Novel Structures and Remarkable Chemisorption  
8 Capacity and Photocatalytic Activity. *Nano Res.* **2011**, *4* (10), 948-962.

9 (35) Telke, A. A.; Kalyani, D. C.; Dawkar, V. V.; Govindwar, S. P. Influence of organic and  
10 inorganic compounds on oxidoreductive decolorization of sulfonated azo dye CI Reactive  
11 Orange 16. *J. Hazard. Mater.* **2009**, *172* (1), 298-309.

12 (36) Galindo, C.; Jacques, P.; Kalt, A. Photodegradation of the aminoazobenzene acid  
13 orange 52 by three advanced oxidation processes: UV/H<sub>2</sub>O<sub>2</sub> UV/TiO<sub>2</sub> and VIS/TiO<sub>2</sub> -  
14 Comparative mechanistic and kinetic investigations. *J. Photoch. Photobio. A.* **2000**, *130* (1),  
15 35-47.

16 (37) Yue, L.; Zhang, X.-M. Structural characterization and photocatalytic behaviors of doped  
17 CeO<sub>2</sub> nanoparticles. *J. Alloys Compd.* **2009**, *475* (1-2), 702-705.

18 (38) Danish, M.; Hashim, R.; Ibrahim, M. N. M.; Sulaiman, O. Characterization of  
19 Physically Activated Acacia mangium Wood-Based Carbon for the Removal of Methyl  
20 Orange Dye. *BioResources* **2013**, *8* (3), 16.

21 (39) Dohčević-Mitrović, Z. D.; Šćepanović, M. J.; Grujić-Brojčin, M. U.; Popović, Z. V.;  
22 Bošković, S. B.; Matović, B. M.; Zinkevich, M. V.; Aldinger, F. The size and strain effects  
23 on the Raman spectra of Ce<sub>1-x</sub>Nd<sub>x</sub>O<sub>2-d</sub> (0 ≤ x ≤ 0.25) nanopowders. *Solid State. Commun.*  
24 **2006**, *137* (7), 387-390.

25 (40) Deacon, G. B.; Phillips, R. J. Relationships between the carbon-oxygen stretching  
26 frequencies of carboxylato complexes and the type of carboxylate coordination. *Coord.*  
27 *Chem. Rev.* **1980**, *33* (3), 227-250.

28 (41) Bauer, C.; Jacques, P.; Kalt, A. Investigation of the interaction between a sulfonated azo  
29 dye (AO7) and a TiO<sub>2</sub> surface. *Chem. Phys. Lett.* **1999**, *307* (5-6), 397-406.

30 (42) Yang, Z.; Wang, Q.; Wei, S.; Ma, D.; Sun, Q. The Effect of Environment on the  
31 Reaction of Water on the Ceria(111) Surface: A DFT+U Study. *J. Phys. Chem. C* **2010**, *114*  
32 (35), 14891-14899.

33 (43) Kundakovic, L.; Mullins, D. R.; Overbury, S. H. Adsorption and reaction of H<sub>2</sub>O and  
34 CO on oxidized and reduced Rh/CeO<sub>x</sub>(111) surfaces. *Surf. Sci.* **2000**, *457* (1-2), 51-62.

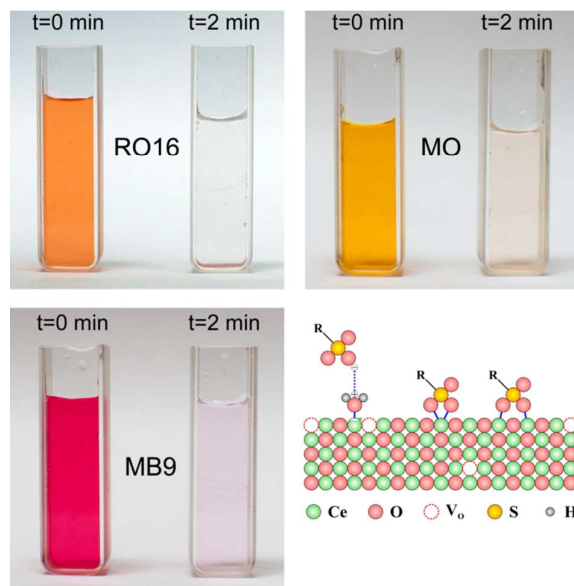
35 (44) Lima, E. C.; Royer, B.; Vagheti, J. C. P.; Simon, N. M.; da Cunha, B. M.; Pavan, F. A.;  
36 Benvenuti, E. V.; Cataluña-Veses, R.; Airoldi, C. Application of Brazilian pine-fruit shell as  
37 a biosorbent to removal of reactive red 194 textile dye from aqueous solution: Kinetics and  
38 equilibrium study. *J. Hazard. Mater.* **2008**, *155* (3), 536-550.

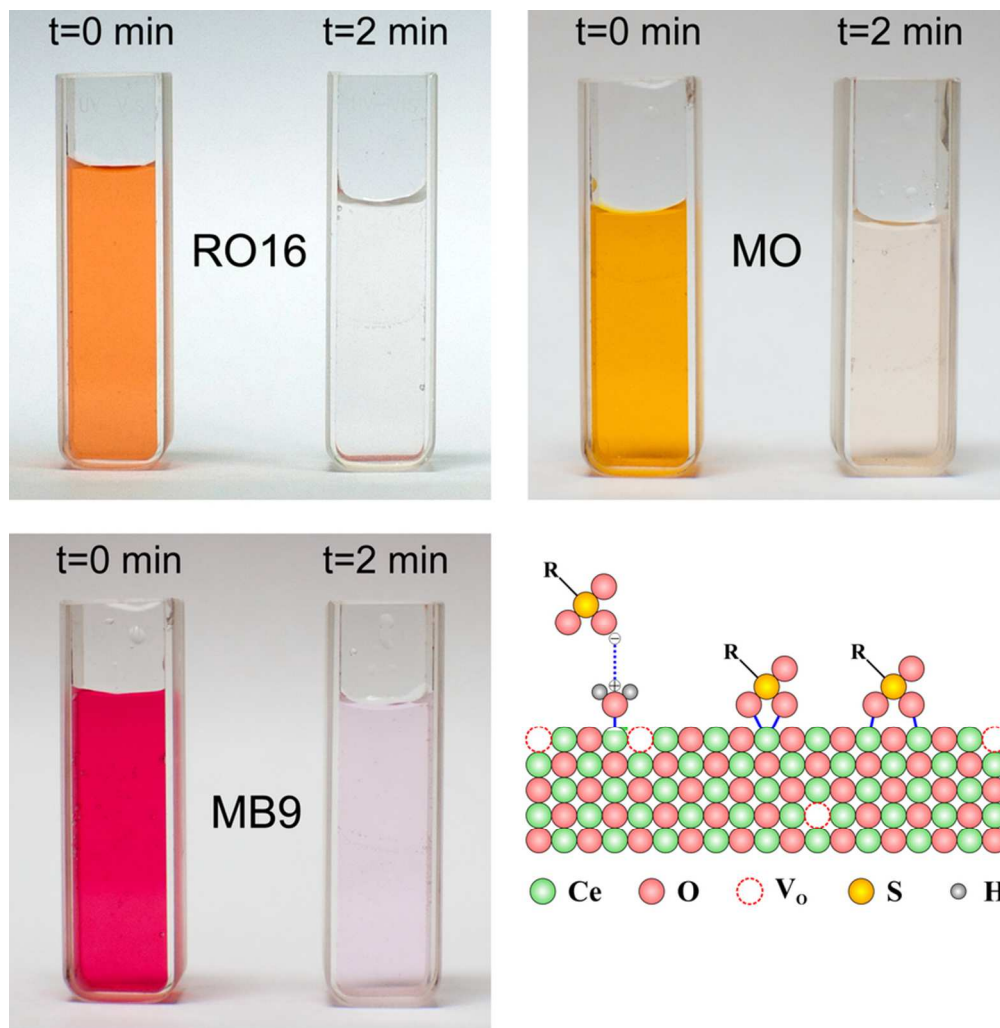
39 (45) Tseng, R.-L.; Wu, F.-C. Inferring the favorable adsorption level and the concurrent  
40 multi-stage process with the Freundlich constant. *J. Hazard. Mater.* **2008**, *155* (1-2), 277-  
41 287.

42 (46) Zhu, Y.-P.; Liu, Y.-L.; Ren, T.-Z.; Yuan, Z.-Y. Hollow manganese phosphonate  
43 microspheres with hierarchical porosity for efficient adsorption and separation. *Nanoscale*  
44 **2014**, *6* (12), 6627-6636.

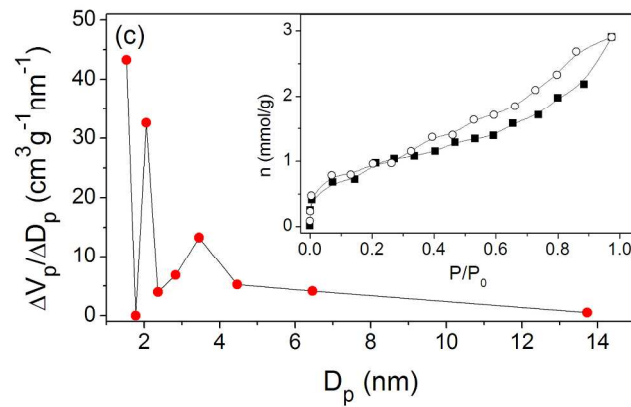
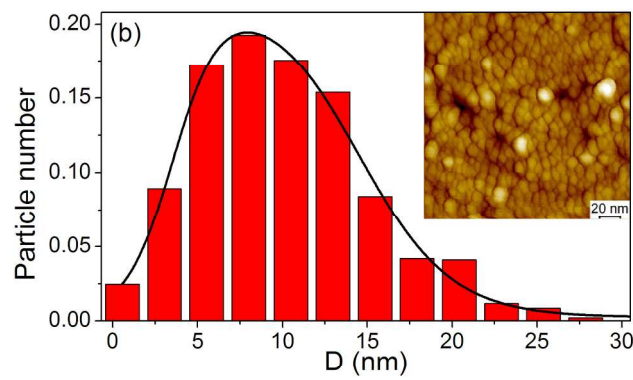
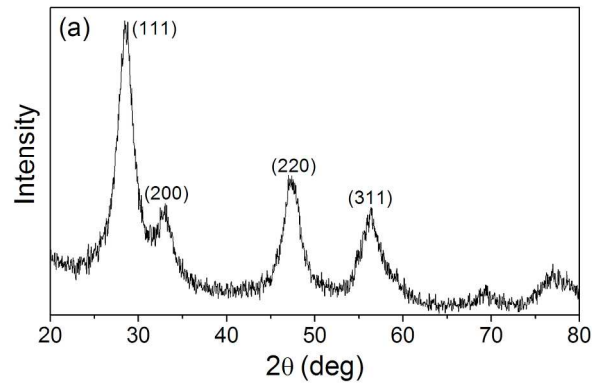
45 (47) Yeddou-Mezenner, N. Kinetics and mechanism of dye biosorption onto an untreated  
46 antibiotic waste. *Desalination* **2010**, *262* (1-3), 251-259.

Figure for TOC

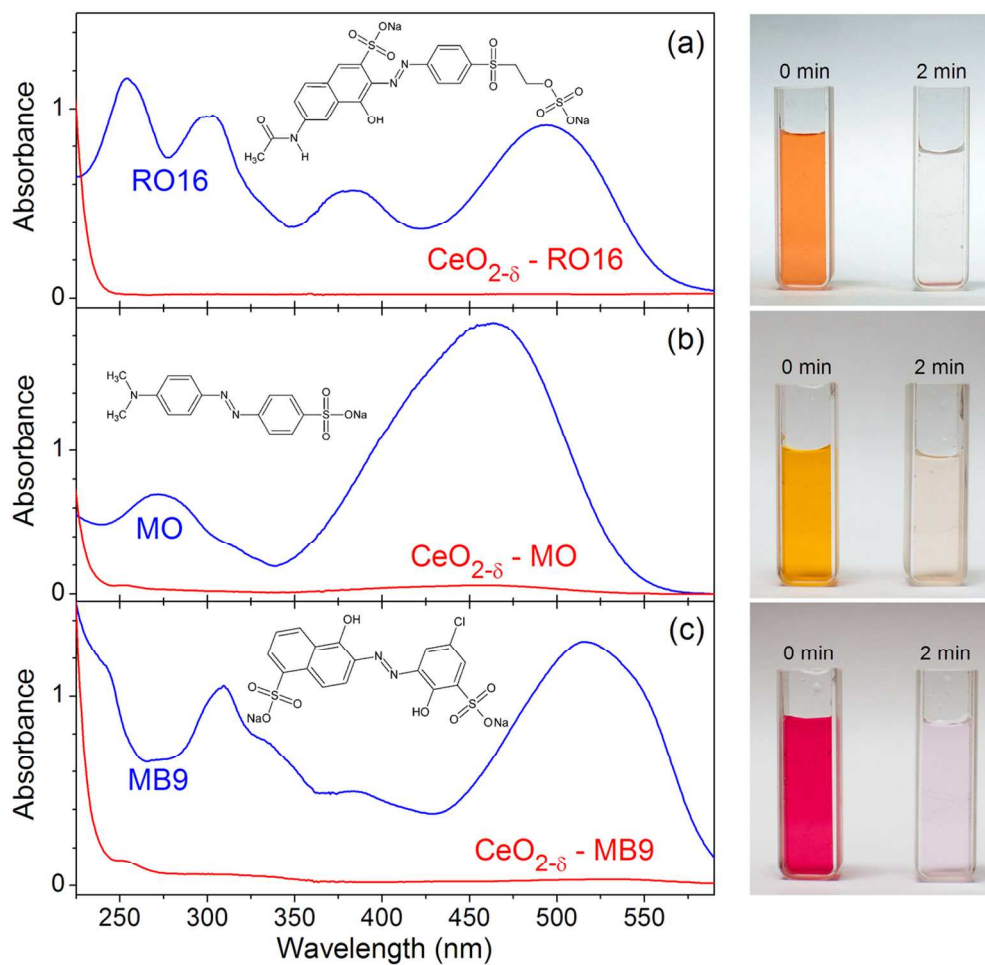




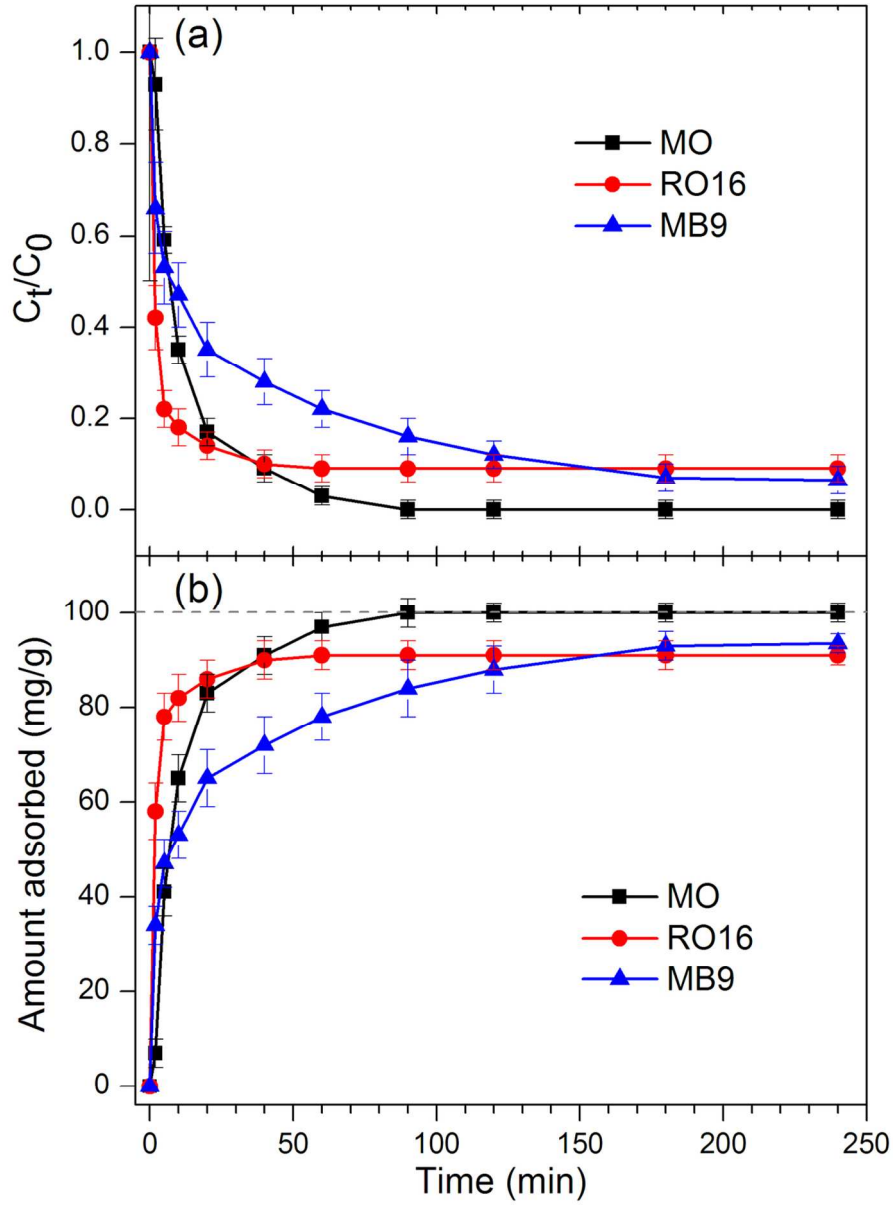
81x83mm (300 x 300 DPI)



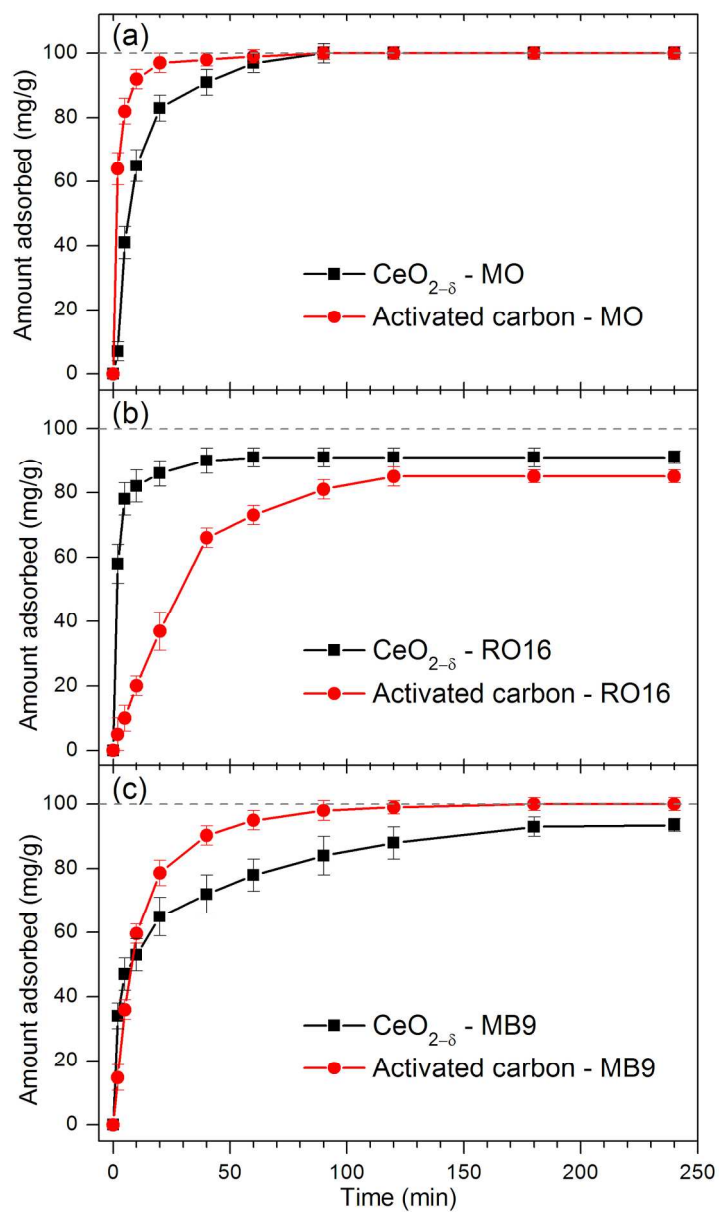
149x277mm (300 x 300 DPI)



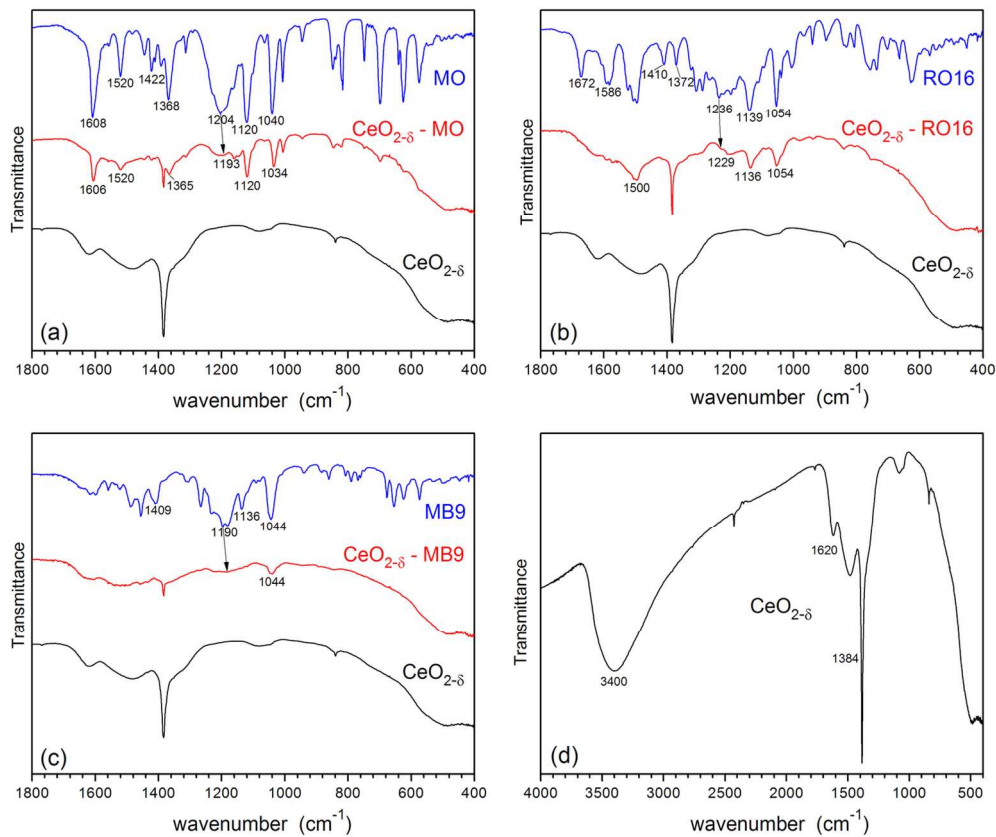
114x109mm (300 x 300 DPI)



107x145mm (300 x 300 DPI)

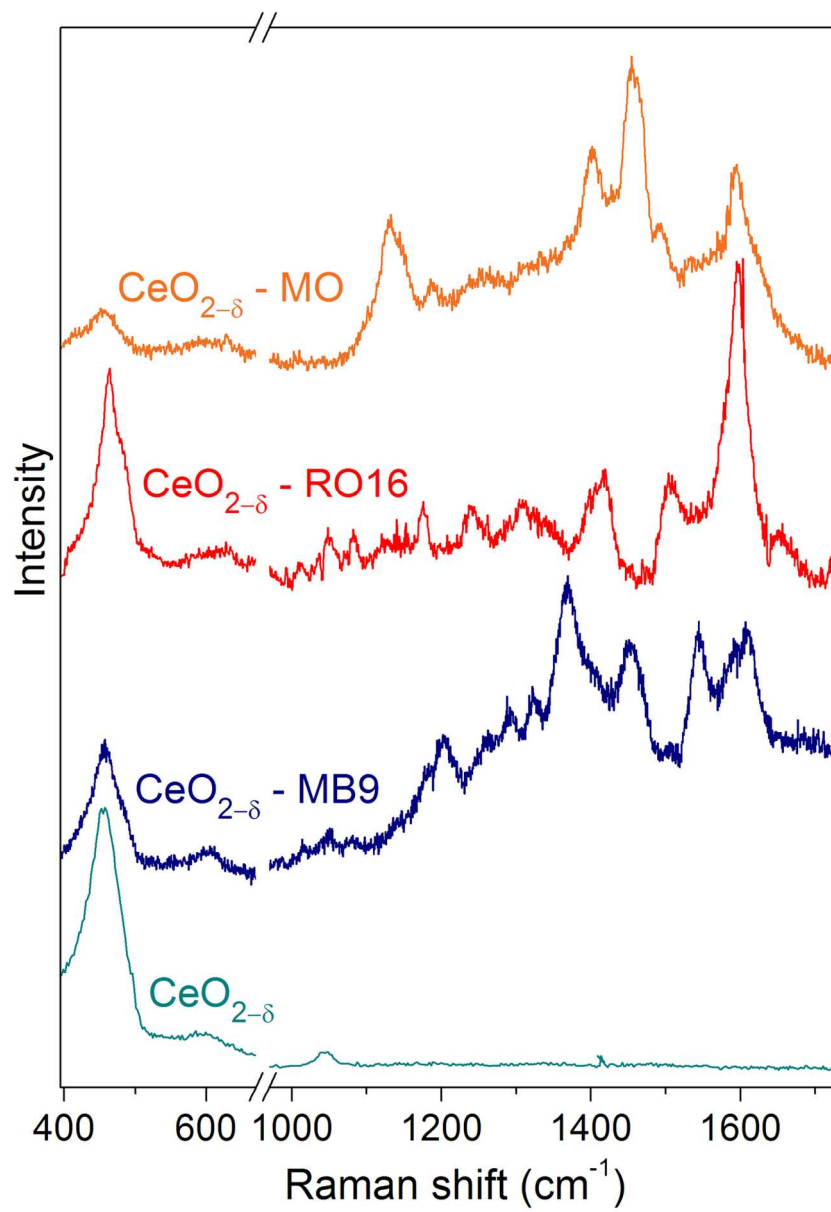


134x226mm (300 x 300 DPI)

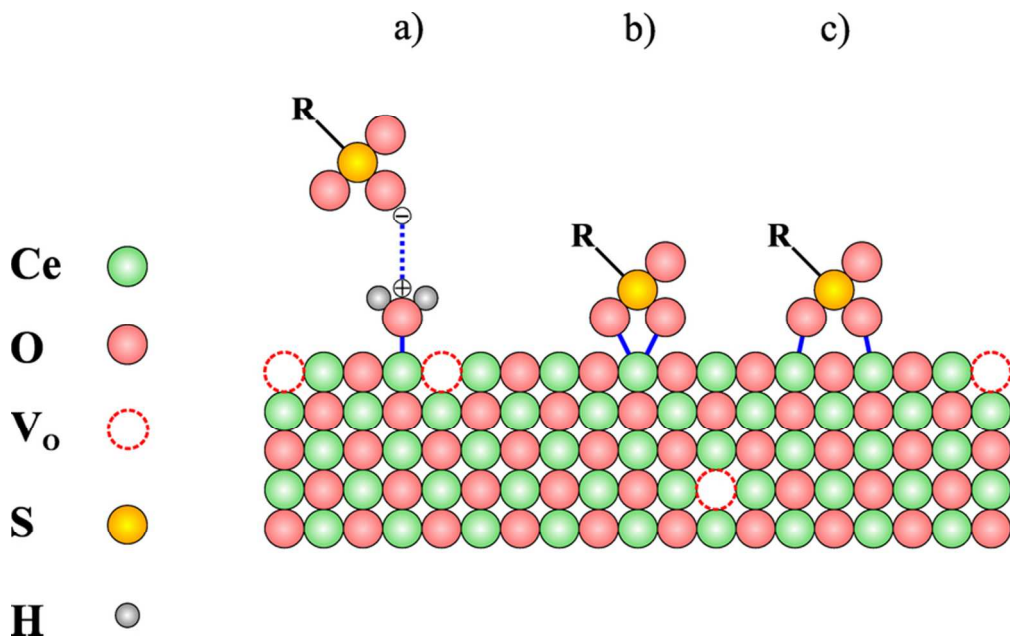


132x110mm (300 x 300 DPI)

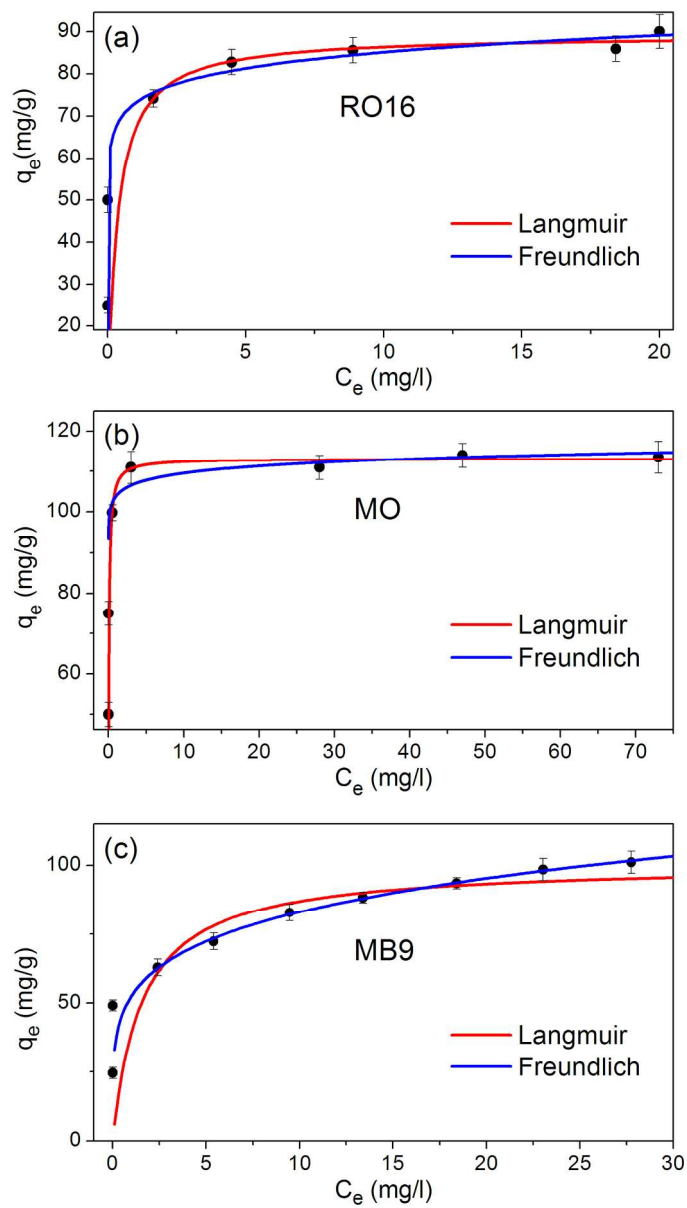




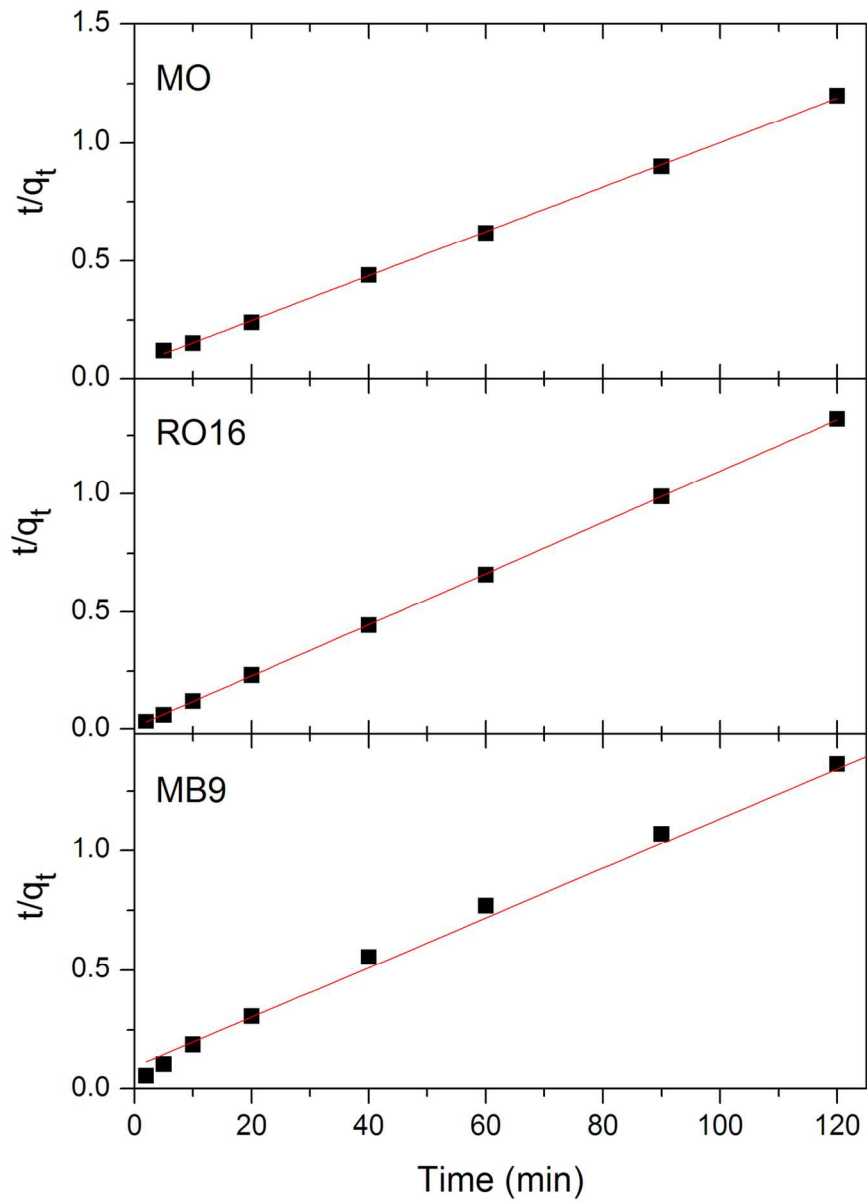
114x164mm (300 x 300 DPI)



74x46mm (300 x 300 DPI)



140x246mm (300 x 300 DPI)



110x152mm (300 x 300 DPI)